

Metal–Organic Framework-Derived Bifunctional Heterojunction Electrocatalysts Embedded in Electrospun Nitrogen-Doped Carbon Nanofibers: Binderless Efficient Freestanding Li-CO₂Mars Pouch Batteries

Ankit Kumar Chourasia,* Keerti M. Naik, and Chandra S. Sharma*

Li-CO₂ batteries offer a revolutionary energy storage solution, combining high specific energy with the utilization of greenhouse CO₂. Although promising for applications on Earth and Mars, the limited cycle life and significant overpotentials from stable discharge products, Li₂CO₃ and amorphous carbon, hinder the practicalization of Li-CO₂ batteries. To address these, a unique freestanding core-shell metal–organic framework-derived heterojunction catalyst, Fe₃O₄/Co₃O₄, embedded in electrospun nitrogen-doped carbon nanofibers for the Li-CO₂Mars batteries, is designed. It eliminates the need for insulating binders, toxic solvents and ensures uniformly distributed composite catalysts across the nanofibers. The electrochemical performance of

Fe₃O₄/Co₃O₄/N-doped carbon fiber (FCo/NCF)-based Li-CO₂Mars coin cells operated in the simulated Mars' atmosphere achieves a cycling life of 120 cycles at a current density of 50 μA cm⁻², with a limited discharge/charge capacity of 0.1 mAh cm⁻², and delivers a full discharge capacity of 6.8 mAh cm⁻² outperforming the conventional catalysts. In situ and first-principle studies demonstrate that enhanced CO₂ adsorption and improved reversibility, driven by the bifunctional catalytic activity of FCo/NCF, lead to exceptional electrochemical performance of Li-CO₂Mars batteries. A prototype of Li-CO₂Mars pouch cell is also developed, operating with an average efficiency of ≈68%, advancing the scalable development of Li-CO₂Mars batteries for diverse applications.

1. Introduction

The growing demand for energy needs and the subsequent global warming due to the excessive CO₂ emissions from the burning of fossil fuels have necessitated the development of alternative environment-friendly renewable energies such as solar and wind energies. However, their dependence on environmental factors requires the development of energy storage systems such as batteries for further use. Li-CO₂ batteries with a specific energy of 1876 Wh kg⁻¹, as per the reaction 4Li + 3CO₂ → 2Li₂CO₃ + C ($E_0 = 2.80$ V), have provided an alternative to the conventional Li-ion batteries, enabling the development of light-weight energy storage devices and, more importantly at the same time, balancing the CO₂ emissions.^[1] Furthermore, Li-CO₂ batteries can potentially serve as a sustainable energy storage system, given that CO₂ comprises the majority of Mars' atmosphere (≈95% by volume) and that the planet is being explored for human habitation.^[2,3] Although Li-CO₂ batteries have significant advantages, several factors have limited their practical applications. Primarily, the formation of the insulating discharge products Li₂CO₃ and amorphous carbon on the reaction

sites impedes the efficient electron transfer from the active sites, lowering the energy efficiency. Moreover, the nonuniform deposition of the discharge products leads to their inefficient decomposition and results in their gradual accumulation on the electrodes. This leads to deactivation of active catalytic sites, thereby reducing the discharge capacity and lowering the cycle life.

Several catalysts have been developed to enhance the CO₂ reduction reaction (CO₂RR) and CO₂ evolution reaction (CO₂ER) through different techniques, such as heterostructure formation,^[3–6] heteroatom doping,^[7–11] employing photocatalysts,^[12,13] and interfacial modification.^[14,15] The various transition metal oxides, sulfides, and carbides as catalysts, along with their composites with carbon, have been used to enhance the CO₂ conversion and improve the dischargeability of the batteries.^[16–21] Despite the improvement, the electrochemical performance of the Li-CO₂ batteries still needs significant advancement to realize their practical development. Co₃O₄, due to its activity for CO₂ reduction along with structural modulation, can be used as the cathode catalyst for Li-CO₂ batteries.^[17] Nonetheless, the inferior catalytic activity for CO₂ER restricts its utilization as an efficient catalyst. To enhance its bifunctional catalytic activity for CO₂RR and CO₂ER, single-atom Ru was implanted on Co₃O₄ nanosheets.^[22] However, there is a need to develop alternate, efficient, and cost-effective catalysts that require replacing expensive noble metals with transition metal-based compounds that are relatively more abundant and economical. Fe₃O₄, having an n-type behavior, can be coupled with the p-type behaving Co₃O₄ to develop a heterostructure with an in-built electric field toward improving the CO₂ reducibility during discharging and decomposition of the discharge products during charging. Among the different techniques such as hydrothermal and^[23]

A. Kumar Chourasia, K. M. Naik, C. S. Sharma
Creative & Advanced Research Based On Nanomaterials (CARBON)
Laboratory
Department of Chemical Engineering
Indian Institute of Technology Hyderabad
Kandi, Sangareddy, Telangana 502285, India
E-mail: ch21resch01007@iith.ac.in
cssharma@che.iith.ac.in

 Supporting information for this article is available on the WWW under <https://doi.org/10.1002/batt.202500224>

reactive sputtering,^[24] employing metal–organic frameworks (MOFs) as a template is one of the most attractive strategies to obtain the metal oxide nanoparticles-porous carbon composites.^[24,25] The zeolitic imidazole framework (ZIF)-based MOF is composed of a metal center (Co, Zn, etc.) connected by the 2-methyl imidazole (linker) (Co (ZIF-67), Zn (ZIF-8), etc.) with bonding angles similar to those of Si—O—Si in zeolites. When pyrolyzed, the organic linker framework is broken down, simultaneously forming uniformly distributed metal oxide nanoparticles.^[26] Nonetheless, despite their advantages regarding catalytic activity, the semiconductor behavior and lower electrical conductivity of the obtained composites restrict their utilization as a standalone electrode material for the Li-CO₂ batteries, necessitating their integration with conductive carbon materials.^[27,28] The different carbon materials, including graphene, carbon nanotubes, reduced graphene oxide, Ketjen black, super-P, etc., can be employed to solve the challenge of electron mobility from the reaction sites to the connecting circuit. However, their complex synthesis process requiring multiple steps and high costs restrict their potential application for large-scale systems.

Incorporating catalysts into 1D electrospun carbon nanofibers offers several benefits, including uniform distribution of catalytically active reaction sites, an electronically conductive network created by the carbon fibers, and an improved three-phase interface for the discharge/charge reaction.^[29] Besides, the electrospun fibers can be directly used as a freestanding electrode, eliminating the need for a binder, toxic solvent N-methyl-2-pyrrolidone (NMP) and preserving the intrinsic catalytically active sites and conductivity of the synthesized catalysts. Further, the side reactions between the reaction intermediates and the binder are prevented, preventing the degradation of the battery system.^[30,31] Additionally, the scalability of the electrospinning technique makes it a suitable technique for developing electrodes for large-scale Li-CO₂ battery systems.

Herein, to integrate the benefits as mentioned earlier, we use a core-shell MOF as a template, electrospun into polyacrylonitrile (PAN)-based nanofibers, followed by carbonization to obtain the Fe₃O₄/Co₃O₄ (FCo) composite nanoparticles uniformly distributed into the N-doped carbon nanofibers (NCFs). The obtained

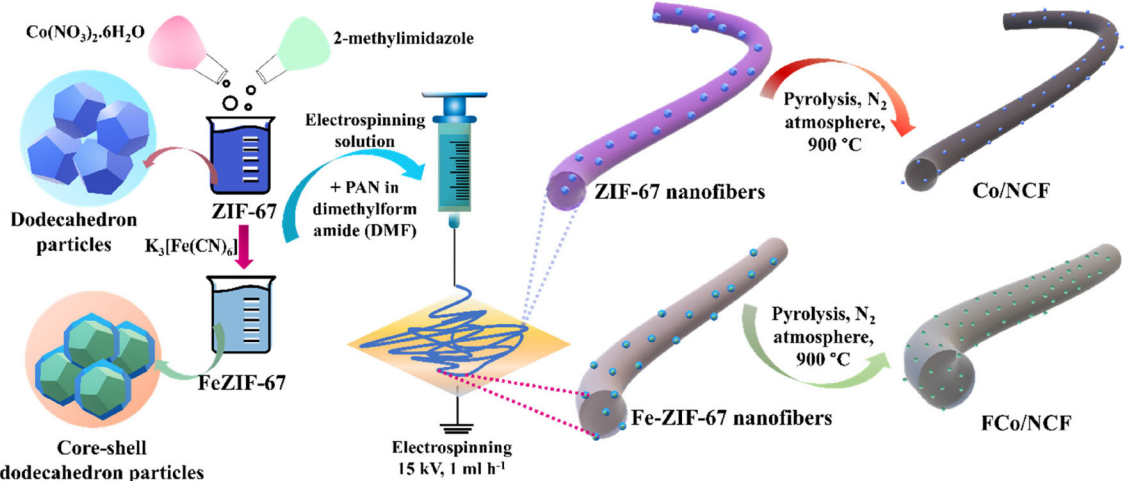
composite catalyst nanofibers were directly used as a freestanding electrode in the Li-CO₂_{Mars} battery. The combination of the 1D electrically conductive network of NCF, along with the improved catalytic activity through the built-in electric field from the composite FCo, enhances CO₂ adsorption. Besides, the formation of Li₂CO₃ discharge products is also significantly enhanced along with their easier decomposition in charging, leading to a high full discharge capacity of 6.8 mAh cm⁻² and Coulombic efficiency of 71.5% at the current density of 50 μA cm⁻². The synergistic catalytic activity leads to a substantially high cycling life of 120 cycles for a limited discharge/charge capacity of 100 μAh cm⁻² with a nearly constant overpotential of 1.57 V even after 80 cycles. Thereafter, we developed a prototype pouch cell Li-CO₂_{Mars} battery operable in Martian gas composition. The developed pouch cell could be operated for nearly 400 h at 50 μA cm⁻² (current: 0.45 mA) with an average energy efficiency of ≈68%. The designed freestanding electrode and the resulting electrochemical performance direct the Li-CO₂_{Mars} battery system's large-scale implementation one step forward on both Earth and Mars.

2. Results and Discussion

2.1. Physicochemical Investigation of the Synthesized Catalysts

The FCo/NCF catalysts were synthesized as per the schematic in Scheme 1.

The characterization studies were subsequently carried out to understand the physicochemical properties of the synthesized catalysts. The field emission scanning electron microscopy (FESEM) images show that the as-synthesized ZIF-67 nanoparticles are uniformly distributed and have a rhombohedral dodecahedron shape (Figure S1a,b, Supporting Information). The Fe-ZIF-67 particles were then synthesized using an anion exchange process. The process involved the interaction between the Co²⁺ ions of the ZIF-67 and the [Fe(CN)₆]³⁻ to form the Co-Fe



Scheme 1. Schematic of the synthesized Co/NCF and FCo/NCF electrocatalysts.

Prussian blue analogue (PBA) nanoparticles on the MOF particles.^[32] The increased roughness of the Fe-ZIF-67 particles, evident in the SEM images in Figure 1a, confirms the formation of a core-shell structure. This is further supported by the high-resolution transmission electron microscopy (HRTEM) analysis, which reveals a thickness of 90–100 nm resulting from the formation of the Co–Fe PBA on the ZIF-67 nanoparticles (Figure 1b, Figure S2a, Supporting Information). Additionally, TEM-energy dispersive spectroscopy (TEM-EDS) mapping images further confirm the Fe shell structure on the core ZIF-67 particles primarily made of Co as well as the presence of the C, N, and O atoms from the linker framework and the cyanide ion (CN^-) of the ferricyanide (Figure S2b–g, Supporting Information).

The different synthesized electrospun PAN-derived carbon nanofibers were further investigated to understand their morphology in the nanofiber framework. The pyrolysis of the electrospun nanofibers leads to the conversion of the PAN to N-doped carbon nanofibers, along with the transformation of the Co metal in the organic framework to Co_3O_4 nanoparticles (Figure S3a, Supporting Information). The TEM analysis shows the distribution of the Co_3O_4 nanoparticles in the NCF framework (Figure S3b, Supporting Information). The observation of the (311) lattice

fringes with a d-spacing of 0.247 nm supports the formation of the Co_3O_4 nanoparticles. Further, the presence of graphitic carbon (101) having a d-spacing of 0.189 nm confirms the integration of the oxide Co_3O_4 with the carbon matrix (Figure S3c,d, Supporting Information). As seen in Figure 1c, the nanosized composite $\text{Fe}_3\text{O}_4/\text{Co}_3\text{O}_4$ nanoparticles that resulted from the MOF breaking down at 900 °C were found to be uniformly enclosed in the fibrous carbon nanofiber network. Further, the TEM analysis shows that the integrated composite nanoparticles are distributed uniformly embedded into the nanofibers (Figure 1d,e). The TEM-EDS mapping also validates the composite's integration and distribution in the nanofibers, along with the presence of nitrogen, indicating the doping of nitrogen in the carbon nanofibers of the material (Figure 1f–k). The HRTEM observation of the (311) plane of Fe_3O_4 (d-spacing: 0.254 nm) with the presence of (220) plane of Co_3O_4 (d-spacing: 0.308 nm) on the graphitic carbon framework ((002) plane, d-spacing: 0.333 nm) confirms the formation of the $\text{Fe}_3\text{O}_4/\text{Co}_3\text{O}_4/\text{NCF}$ composite (Figure S4, Supporting Information). The formation of the composite heterostructure between Fe_3O_4 and Co_3O_4 is further evidenced by the increased interplanar spacing of the (220) plane of Co_3O_4 compared to the standard d-spacing of 0.285 nm, which

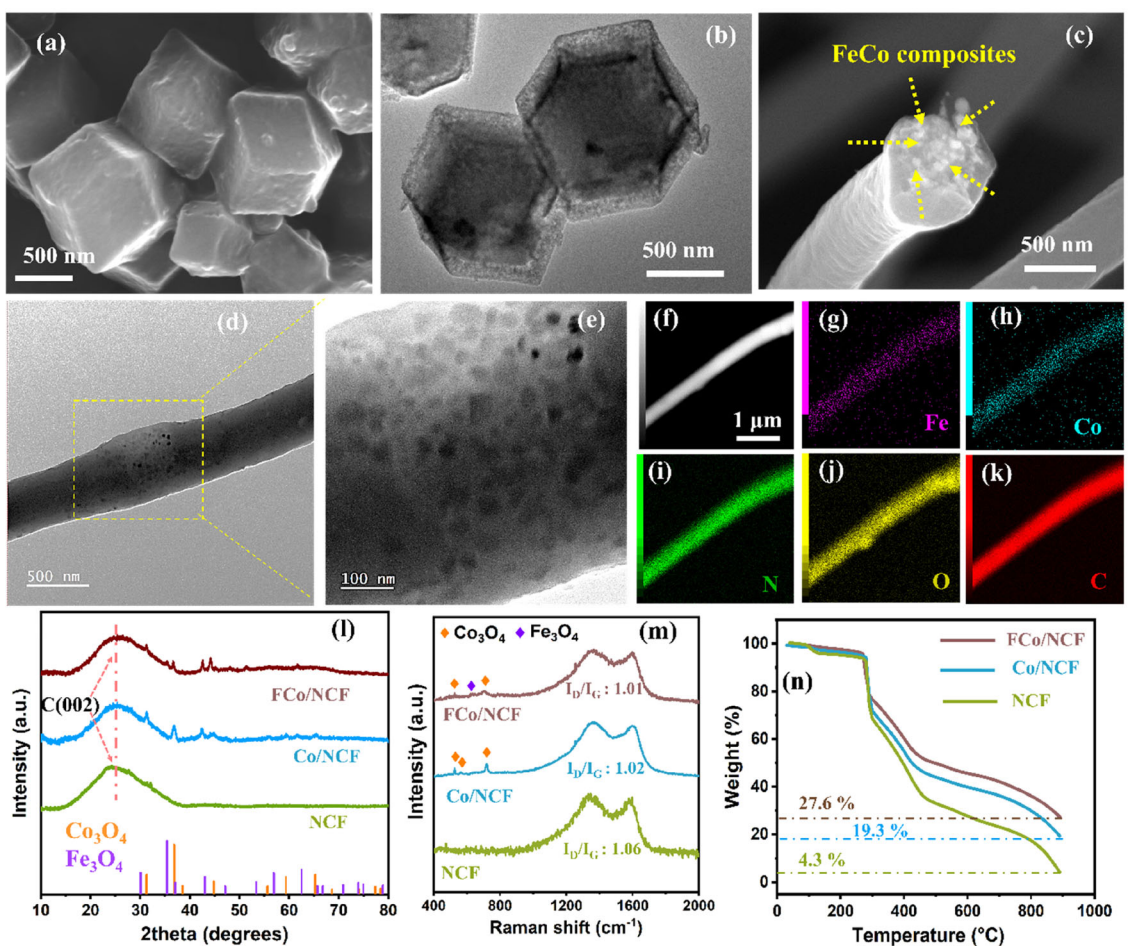


Figure 1. a) FESEM and b) TEM images of the synthesized Fe-ZIF-67 particles. c) FESEM and d,e) TEM and HRTEM images of the electrospun FCo/NCF. f) STEM image, g) Fe, h) Co, i) N, j) O, and k) C are the corresponding elemental mapping images of the FCo/NCF. l) XRD patterns (JCPDS file numbers of Co_3O_4 : 00-042-1467; Fe_3O_4 : 03-065-3107), m) Raman spectra, and n) TGA curves of the synthesized NCF, Co/NCF, and FCo/NCF catalysts.

results from lattice strain and distortion induced by the heterojunction with Fe_3O_4 .^[33,34] Thus, the uniform distribution of the composite nanoparticle embedded, along with its integration with the NCF, will provide substantial catalytically active reaction sites for the CO_2RR and CO_2ER . Moreover, it will efficiently transfer electrons from the active sites to the external circuit through the composite fibrous carbon framework.

X-ray diffraction (XRD) analysis is carried out to investigate the crystallographic properties of the different samples. The diffraction peaks of the synthesized ZIF-67 dodecahedron structure matched with the standard peaks of ZIF-67, confirming the formation of the MOF. Further, the diffraction patterns of Fe-ZIF-67 confirmed the formation of Co-Fe PBA on the ZIF-67 nanoparticles (Figure S5, Supporting Information). The pyrolysis of the electrospun nanofibers led to the decomposition of the MOF along with the polymer PAN and subsequent conversion of the Fe-ZIF-67 to a composite of $\text{Fe}_3\text{O}_4/\text{Co}_3\text{O}_4/\text{NCF}$. Simultaneously, the ZIF-67 converted completely to the $\text{Co}_3\text{O}_4/\text{NCF}$ (Figure 1l). The average particle size of the Co_3O_4 was further obtained from the particle size distribution analysis using the TEM images to be ≈ 10.7 nm. In contrast, the average particle size of $\text{Fe}_3\text{O}_4/\text{Co}_3\text{O}_4$ (FCo) nanoparticles was ≈ 23.7 nm, confirming the formation of the composite between Fe_3O_4 and Co_3O_4 (Figure S6, Supporting Information). Furthermore, a comparison of the fiber diameters among the synthesized catalysts reveals a significant reduction in the diameter of Co/NCF relative to NCF, likely due to the catalytic enhancement of polymer decomposition during pyrolysis.^[35] In contrast, FCo/NCF exhibited a notable increase in fiber diameter compared to NCF, which may be attributed to the larger overall size of the $\text{Fe}_3\text{O}_4/\text{Co}_3\text{O}_4$ composite nanoparticles compared to those of Co_3O_4 alone (Figure S7, Supporting Information).

Further, a higher graphitic nature ensures greater electrical conductivity for the movement of electrons from the reaction sites to the external circuit. The degree of graphitization of the synthesized nanofibers was initially investigated using Raman spectroscopy. As can be observed from the obtained Raman spectra, the I_D/I_G ratio of the FCo/NCF (≈ 1.01) was reduced compared to that for NCF (≈ 1.06) while being nearly similar to Co/NCF, indicating the enhancement of the graphitic structure with the addition of the MOF-derived nanoparticles into the NCF (Figure 1m). The improved graphitization is due to the addition of iron and cobalt, which catalyzes the amorphous carbon to graphitic carbon at temperatures of 800–900 °C.^[36–39] Moreover, the different peaks of Fe_3O_4 and Co_3O_4 can be observed in the range of 500 to 800 cm⁻¹, confirming the integration of the composite in the carbon nanofiber network. The thermogravimetric analysis (TGA) carried out for the electrospun PAN-MOF composite nanofibers in an N_2 atmosphere reveals a slight loss in the mass of the nanofibers around 100 °C from the loss in moisture. Further, a sharp decrease in weight loss is observed around 280 °C due to the cyclization of the nitrile groups ($\text{C}\equiv\text{N}$) to $\text{C}=\text{N}$ present in the polyacrylonitrile fibers called the oxidative stabilization process.^[40,41] Subsequently, carbonization of the stabilized fibers starts at a temperature >400 °C, resulting in significant mass loss, as can be observed in all the synthesized nanofibers. After carbonization at 900 °C, the obtained NCF weighed 4.3%,

indicating significant weight loss. In contrast, adding the various MOFs to the electrospun fiber network improves the fiber stability and confirms the presence of nanocomposites in the fibers, as evidenced by the final weight of the FCo/NCF ($\approx 27.6\%$) and Co/NCF ($\approx 19.3\%$) (Figure 1n). The four-probe electrical conductivity measurements were then conducted to investigate the effect of graphitization on the conduction of electrons of the synthesized electrospun materials. The electrical conductivity of the FCo/NCF was calculated to be 32.8 S m⁻¹, while that for Co/NCF was 23.7 S m⁻¹. In contrast, NCF's electrical conductivity was only 10.1 S m⁻¹, demonstrating that the metal-based nanoparticles' catalytic graphitization enhanced the electrical conductivity, permitting the efficient flow of electrons from the reaction sites to the external circuit (Figure 2a). N_2 adsorption-desorption was carried out to investigate the available surface area for the electrochemical reactions along with the pore structure of the synthesized NCF, FCo/NCF, and Co/NCF catalysts. The obtained isotherms are of the type-IV isotherms with hierarchical porous structures comprising micro- and mesopores. A high surface area of 151.3 m² g⁻¹ was observed for the synthesized NCFs. The reduction in the surface area to 29.4 and 7.4 m² g⁻¹ for the FCo/NCF and Co/NCF, respectively, confirms the incorporation of the MOF-derived nanoparticles in the pores of the NCF (Figure 2b, Figure S8a, Supporting Information). In addition, the pore size distribution and the observance of a similar H3 hysteresis loop in the isotherms of the synthesized freestanding electrodes confirm the presence of a combination of micro- and mesopores.^[42] Moreover, the similar pore size distribution of the NCF confirms the preservation of the porous nature of NCF in the composite FCo/NCF. The presence of this hierarchical porosity enables the efficient interaction between the reactants, Li^+ ions and CO_2 molecules in the three-phase interface, while the mesoporous structure provides sufficient space for the accommodation of the discharge products (Figure S8b and S9, Supporting Information).

X-ray photoelectron spectroscopy (XPS) studies were conducted to understand the surface chemical properties of the different fibers. The broad spectra in Figure 2c confirm the presence of the C, N, O, Co, and Fe in FCo/NCF, the same elements except Fe in the case of Co/NCF, and the rest of the elements except the metallic elements in NCF. Furthermore, XPS elemental analysis indicated that the Fe_3O_4 and Co_3O_4 contents in the FCo/NCF composite were $\approx 4.6\%$ and 5.3% by mass, respectively. These values are consistent with the mass concentration of the precursor Fe-ZIF67 incorporated in the composite precursor electrospinning gel. In the case of Co/NCF, the Co_3O_4 content was about 9.3% by mass, which corresponds to the proportion of ZIF67 precursor integrated into the electrospun nanofiber matrix, as mentioned in the experimental sections. The high-resolution Fe 2p XPS spectra confirmed the formation of Fe_3O_4 with the presence of Fe^{3+} corresponding to the Fe^{2+} of Fe 2p_{3/2} peaks at 710 and 713.5 eV, respectively. In addition, there was a right shift of 1.1 eV of the Fe 2p_{1/2} peak corresponding to the Fe^{3+} compared to the standard observable peak at 723.5 eV^[43] (Figure 2d). The increase in the binding energy arises due to the shift in electron density from the lower electronegative Fe atoms (1.83) to higher electronegative Co atoms (1.88), indicating the formation of the

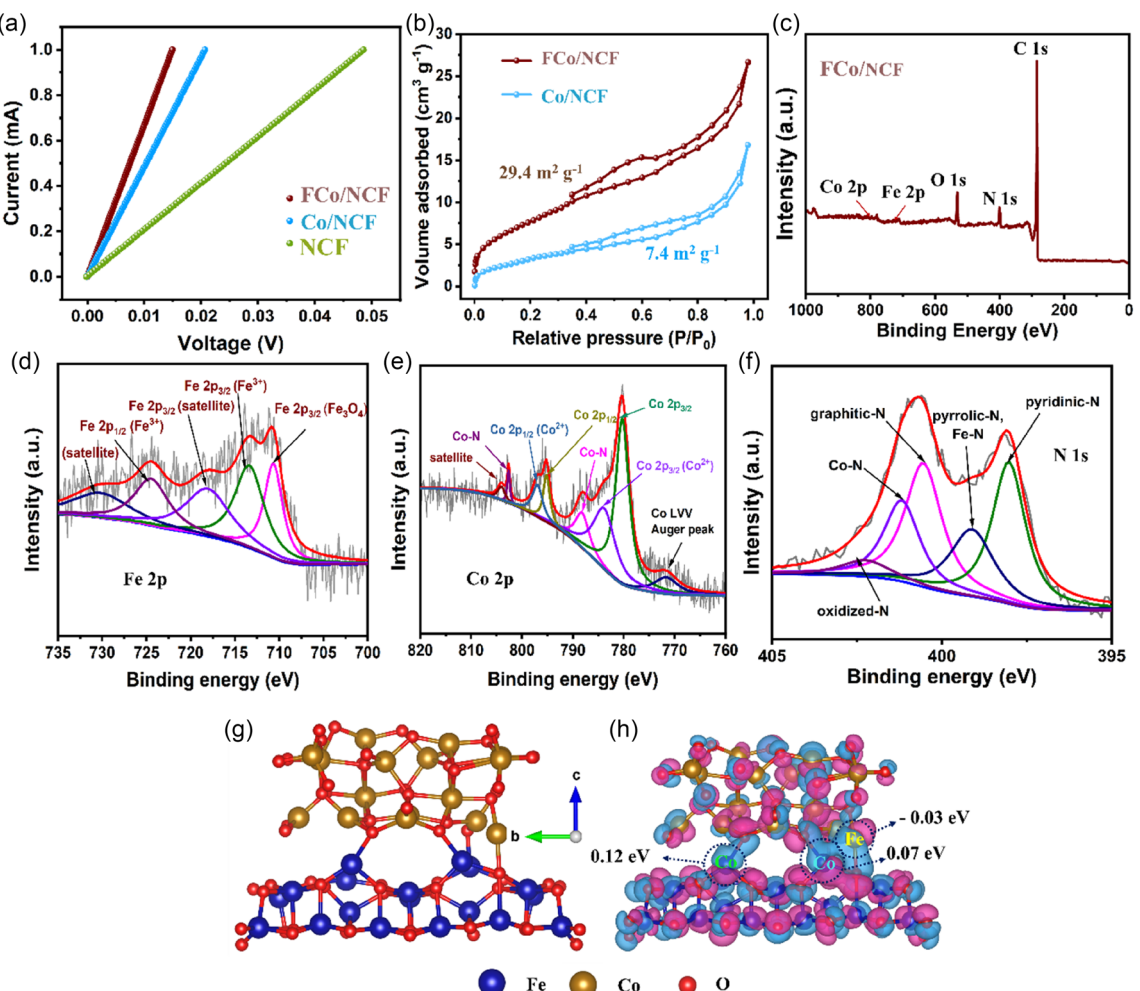


Figure 2. a) Electrical conductivity through the four-probe method curves of the synthesized NCF, Co/NCF, and FCo/NCF catalysts. b) N_2 adsorption-desorption isotherm of the synthesized FCo/NCF and Co/NCF catalysts. c) Wide spectra, high-resolution, d) Fe 2p, e) Co 2p, and f) N 1s XPS spectra of the synthesized FCo/NCF catalysts. g) The composite catalyst structure, and h) the corresponding charge density difference plot (blue color represents positive charge density, while the pink color represents negative charge density).

Fe_3O_4 - Co_3O_4 composite and the development of a built-in electric field heterojunction. The high-resolution Co 2p XPS spectra can be divided into Co^{2+} and Co^{3+} of Co 2p_{3/2} and Co 2p_{1/2} peaks (Figure 2e).

Moreover, Co-N peaks can also be observed at 788.4 and 802.5 eV, corresponding to Co 2p_{3/2} and Co 2p_{1/2}, respectively, indicating the synergistic interaction between the composite and the N-atom in the NCF.^[44] The deconvolution of the N 1s spectra (Figure 2f) reveals the presence of pyridinic-N, pyrrolic-N, graphitic-N, and small amounts of oxidized-N along with the observation of Fe-N and Co-N, indicating the N-doping along with the interaction between the Fe_3O_4 - Co_3O_4 composite. Moreover, a significant increase in the nitrogen content was observed for FCo/NCF to 7.7% (by mass) compared to the NCF (6.1%), possibly due to the N from the decomposition of the imidazole framework and the cyano group of the PBA. The substantial increase in the pyridinic nitrogen content of the FCo/NCF and Co/NCF compared to the NCF signifies the increased electrical conductivity and reactivity of the MOF-derived NCFs. The deconvolution of the C 1s XPS spectra (Figure S10a,

Supporting Information) reveals the presence of interaction between the metal atoms and the carbon atoms along with the C=N bonds, implying the N-doping into the graphitic carbon framework of the host NCF (Figure S10–S12, Supporting Information). The deconvolution of the O 1s XPS spectra of the FCo/NCF further confirms the presence of Fe_3O_4 and Co_3O_4 in the synthesized composite electrocatalysts (Figure S10b, Supporting Information). We further carried out first-principles theoretical studies using density functional theory (DFT) to understand the intrinsic properties of the composite catalyst Fe_3O_4 / Co_3O_4 . The density of states (DOS) and charge transfer analysis were initially performed on the composite catalyst Fe_3O_4 (220)/ Co_3O_4 (220) (FCo) to understand the electronic behavior and their reactivity. A significant increase in the reactivity of the composite can be observed by the lowering of the Fermi level of FCo (E_F : -6.19 eV) compared to Co_3O_4 (E_F : -6.24 eV) and Fe_3O_4 (E_F : -6.54 eV). Moreover, the charge density and Bader charge analysis revealed an increase in the charge on the Co atoms at the interface by 0.07–0.12 eV. Comparatively, a decrease in the charge by 0.03 eV was observed for the Fe atom, implying a

synergistic electron transfer and building up of a heterojunction internal local electric field, which modulates the electronic properties of the composite catalyst similar to the observations in the physicochemical characterizations (Figure 2g,h, Supporting Information).

2.2. Electrochemical Performance of the Li-CO₂Mars Batteries

The different synthesized carbon nanofibers (FCo/NCF, Co/NCF, and NCF) were used directly as the freestanding electrodes and assembled into a CR2032 coin-cell assembly to investigate the electrochemical performance of the Li-CO₂Mars batteries. Understanding the intrinsic reaction kinetics is the first step toward investigating the catalytic behavior and subsequent effects on the battery performance. Cyclic voltammetry studies conducted in the potential range of 2.0–4.5 V at the scan rate of 0.1 mV s⁻¹ demonstrated the onset of CO₂ reduction reaction

≈3.0 V, with the reduction peaks in the range of 2.3–2.4 V (Figure 3a). The highest peak reduction current observed for the FCo/NCF demonstrated the enhanced CO₂RR catalytic activity through the formation of synergistic composite of Fe₃O₄/Co₃O₄ with the N-doped CF. Similarly, CO₂ER catalytic activity influences the overpotential and, subsequently, the cyclability of the Li-CO₂Mars batteries. A prominent peak at 3.74 V corresponding to the decomposition of the discharge products as per the reaction, $2\text{Li}_2\text{CO}_3 \rightarrow 4\text{Li}^+ + 2\text{CO}_2 + \text{O}_2 + 4\text{e}^-$, was observed in the case of the FCo/NCF.^[9,45] In contrast, no prominent reduction peaks are observed for Co/NCF and NCF, which signifies the enhanced CO₂ER catalytic activity of FCo/NCF. Full discharge/charge studies were carried out at the current density of 50 μA cm⁻² to investigate the extent of complete dischargeability of the system. A significantly high discharge capacity of 6.8 mAh cm⁻² was observed, and the battery can be recharged

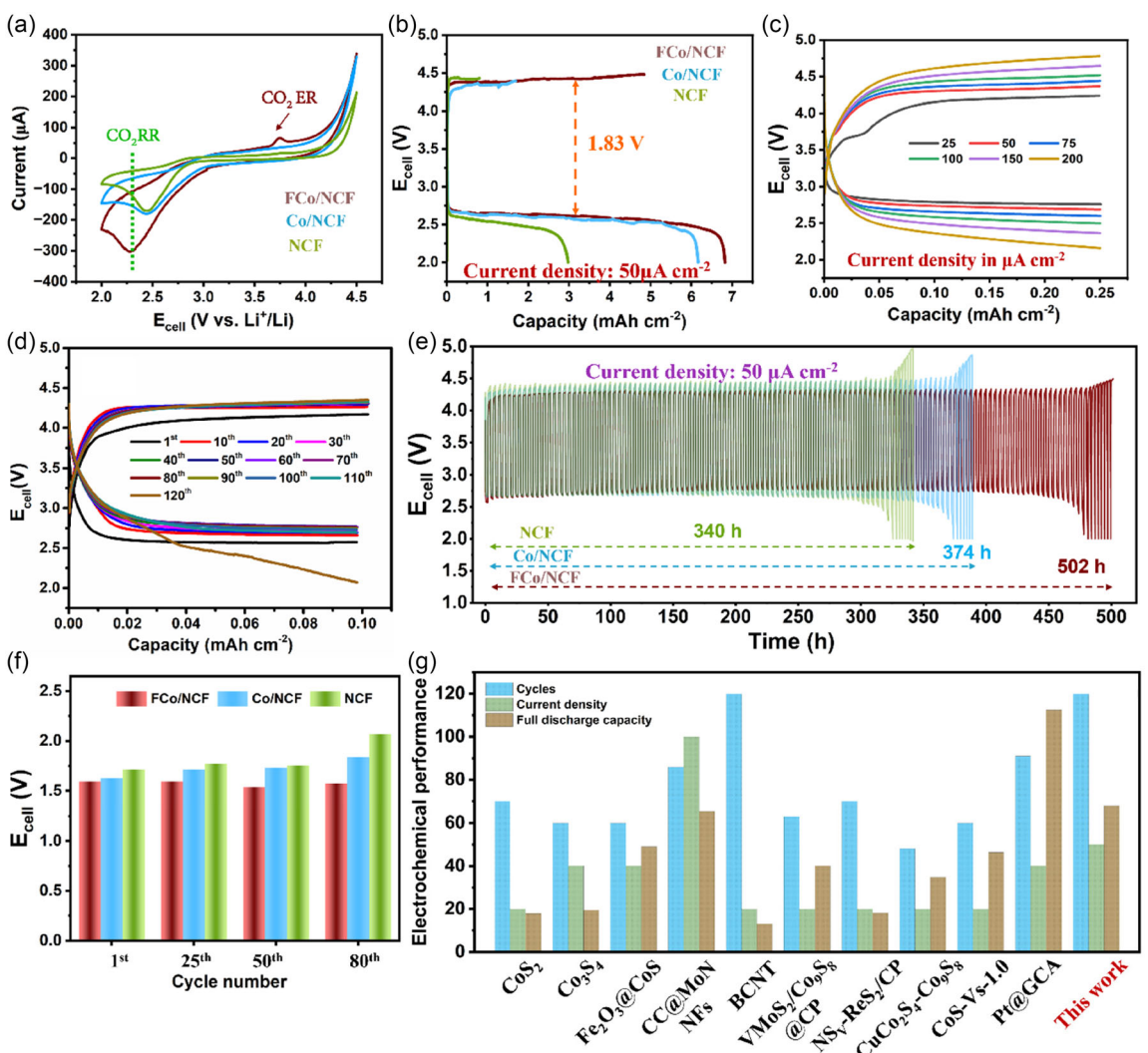


Figure 3. a) Cyclic voltammetry curves at the scan rate of 0.1 mV s⁻¹. b) Full discharge/charge curves of the FCo/NCF, Co/NCF, and NCF-based Li-CO₂Mars batteries. c) Rate capability at different current densities. d) Long-term cycling curves (E vs. capacity) of the FCo/NCF-based Li-CO₂Mars batteries at the current density of 50 $\mu\text{A cm}^{-2}$ for a limited capacity of 0.1 mAh cm^{-2} . e) E versus t curves and f) overpotential at the different cycle numbers for the FCo/NCF, Co/NCF, and NCF-based Li-CO₂Mars batteries. g) Comparison of the recent literature corresponding to the different electrochemical performances (full discharge capacity in mAh cm^{-2} (the values are scaled 10 times for comparison), number of cycles, current density in $\mu\text{A cm}^{-2}$ of cycling) of the different freestanding electrodes (Table S1, Supporting Information).

with a reversible Coulombic efficiency of 71.5% (Figure 3b). Comparatively, Co/NCF can be discharged to a capacity of 6.1 mAh cm^{-2} , while the NCF can be discharged to only 3 mAh cm^{-2} . Despite the high discharge capacities of Co/NCF and NCF, the completely discharged electrodes can be reversed only with reversible coulombic efficiencies of 27.2% and 26%, respectively. The rate capability studies with different current densities were then carried out with a cutoff capacity of 0.25 mAh cm^{-2} to assess the operability of the designed system at varying current loads. The FCo/NCF-based Li-CO₂Mars battery can be efficiently operated till the current density of $50\text{--}200 \mu\text{A cm}^{-2}$ with the terminal discharge voltage of 2.2 V even at the high current density of $200 \mu\text{A cm}^{-2}$, confirming the effect of the catalytic activity on the battery performance (Figure 3c). In contrast, the Co/NCF and the NCF-based Li-CO₂Mars batteries could not be effectively operated for the cutoff discharge capacity at the current densities of 150 and $200 \mu\text{A cm}^{-2}$, indicating the combined effect of the composite catalyst on the reversibility of the system (Figure S13, Supporting Information). Further, cycling studies were carried out at the current density of $50 \mu\text{A cm}^{-2}$ for the limited discharge capacities of 0.1 mAh cm^{-2} to assess the long-term operability of the Li-CO₂Mars batteries. The FCo/NCF-based Li-CO₂Mars battery can be cycled to more than 120 cycles with an operational life of 502 h, while the Co/NCF and NCF were able to cycle up to 94 and 80 cycles along with an operational life of 374 and 340 h, respectively (Figure 3d,e, Figure S14, Supporting Information). Further, a comparison of the operating overpotential during cycling of the different synthesized freestanding Li-CO₂Mars batteries reveals a constant overpotential of 1.57 V for the FCo/NCF-based Li-CO₂Mars battery.

In comparison, the overpotential of the Co/NCF significantly increased from 1.62 V in the first cycle to 1.84 V in the 80th cycle, while the overpotential of the NCF-based Li-CO₂Mars battery increased substantially from 1.71 V in the first cycle to 2.07 V, leading to cell failure after 80 cycles (Figure 3f). Additionally, even at the increased limited discharge/charge capacity of 0.25 mAh cm^{-2} , the FCo/NCF could be cycled to 60 cycles with an operational life of 620 h compared to the 42 cycles of Co/NCF for 436 h, indicating the improved catalytic behavior from the incorporation of Fe. In comparison, NCF could only be cycled to 11 cycles for 124 h due to their significantly low catalytic ability for catalyzing the discharge/charge reactions (Figure S15, Supporting Information). Thus, the synergistic combination of the NCF and uniform distribution of the composite Fe₃O₄-Co₃O₄ nanoparticles coupled with their enhanced catalytic activity for the CO₂RR and CO₂ER due to the heterojunction formation leads to a significantly improved Li-CO₂Mars battery compared to the recently reported catalysts (Figure 3g, Table S1).

2.3. Investigation of the Catalytic Effect in Li-CO₂Mars Batteries

The excellent electrochemical performance of the Li-CO₂Mars batteries needs further investigation of the intricate reactions on the freestanding electrodes during the discharged/charged state to understand the catalytic effect on the CO₂RR and CO₂ER. Physicochemical characterizations such as XRD, Raman, and

SEM analysis were conducted to understand the discharge/charge behavior during the operation of the different NCF-based Li-CO₂Mars batteries. XRD analysis confirmed the formation of the Li₂CO₃ (JCPDS: 01-072-1216) as per the discharge reaction, $4\text{Li}^+ + 3\text{CO}_2 \rightarrow 2\text{Li}_2\text{CO}_3 + \text{C}$, and its subsequent complete decomposition on recharging (Figure 4a). Electrochemical impedance spectra (EIS) studies further confirmed the formation and decomposition of the discharge products. The charge-transfer resistance (R_{ct}) significantly increased from 135Ω in the pristine state to 266Ω in the discharged state, indicating the formation of the insulating discharge products.

Further, as the battery was recharged, the R_{ct} decreased to 192Ω , indicating the decomposition of the discharge products (Figure 4b). The FESEM analysis reveals the formation of the platelet-like structure discharge products on the FCo/NCF uniformly covering the fiber surface (Figure 4c). In comparison, the Co/NCF was covered with sheets like discharge products growing beyond the fiber surface. Similarly, severe sheet-like layers of discharge product formation were observed for NCF, indicating the deactivation of the active sites. Subsequent recharging of the system led to the complete decomposition of the discharge products formed on the FCo/NCF. Contrastingly, accumulated lumps of the discharge products can still be observed for Co/NCFs, while a thin sheet-like discharge product covers the surface of NCF (Figure S16 and S17, Supporting Information). The presence of the discharge products on the Co/NCF and NCF even after recharging is due to the lower catalytic activity compared to FCo/NCF, which, owing to the gradual accumulation over the cycles, will lead to a reduced operational life. The Raman spectroscopy studies further confirm the observation, where the I_D/I_G ratio significantly increases to 1.29 and 1.54 for Co/NCF and NCF due to the discharge product formation. Subsequently, recharging the system, although it leads to a reduction in the ratio to 1.13 for Co/NCF and 1.19 for NCF, is still significantly higher compared to the 1.03 for the FCo/NCF (Figure S18, Supporting Information).

Despite the observation of Li₂CO₃ in the discharge products by XRD analysis, the presence of carbon in the discharge products has been doubtful due to the presence of a trace amount of O₂ with the CO₂ gas (1:595 by volume) as the formed carbon may react with the intermediate radicals to form CO and CO₂. To further understand the formation and subsequent decomposition of carbon during discharging and charging, respectively, we conducted *in situ* Raman spectroscopy studies with the Martian gas composition at intervals of an hour for discharging the system to 0.25 mAh cm^{-2} at the current density of $50 \mu\text{A cm}^{-2}$ (Figure 4e,f).

It can be observed from the obtained Raman spectra that, as the discharge reaction proceeded, there was a gradual formation of amorphous carbon evident with the increase in the I_D/I_G ratio as per the widely reported discharge reaction, $4\text{Li}^+ + 3\text{CO}_2 \rightarrow 2\text{Li}_2\text{CO}_3 + \text{C}$ (amorphous). Subsequently, with the recharging of the system, the I_D/I_G ratio declined to a nearly pristine state, revealing the decomposition of the formed carbon and restoration of the active sites for subsequent cycles. Further, the DFT studies were carried out to understand the reaction mechanisms and their influence by the designed electrocatalyst.

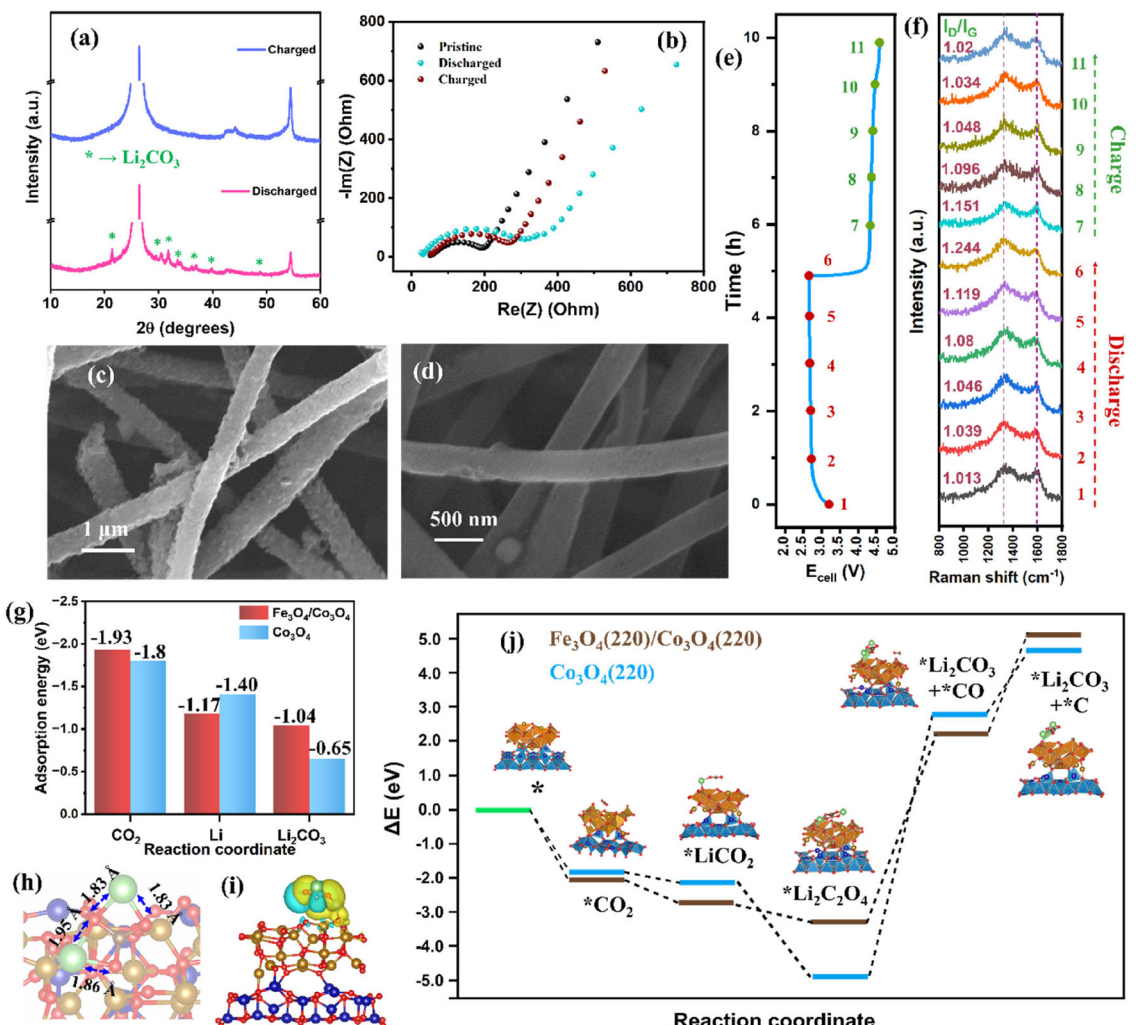
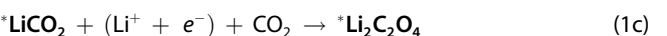


Figure 4. a) XRD pattern of the discharged and charged electrodes FCo/NCF-based Li-CO₂Mars battery. b) EIS of the pristine, discharged, and charged electrodes. FESEM images of the FCo/NCF in the c) discharged and d) charged state. e) E_{cell} versus t curve and the corresponding f) *in situ* Raman spectra of the FCo/NCF-based Li-CO₂Mars battery. g) Comparison of the adsorption energies of Li, CO₂, and Li₂CO₃; h) different bond lengths in adsorbed Li₂CO₃ on the substrate catalyst; and i) the corresponding charge density difference plot on the composite catalyst (yellow represents positive charge density; cyan represents negative charge density). j) Reaction pathway for the discharge reaction in MOF-derived nanoparticles/carbon nanofiber electrocatalysts-based Li-CO₂Mars batteries.

The modulated electronic properties result in enhanced CO₂ adsorption of the FCo catalyst surface compared to the Co₃O₄. Comparatively, the adsorption energy of Li for both the catalysts is lower than the CO₂ adsorption, indicating the discharge reaction to proceed with the interaction between adsorbed CO₂ and Li. The higher adsorption energy of Li₂CO₃ arising from the modified electronic structure of the composite leads to the favorable formation of the discharge product compared to the Co₃O₄ (Figure 4g). The heterojunction catalyst enhances the interaction between the discharge product, Li₂CO₃, and the substrate catalyst. This can be identified from the elongation of the Li—O bond length to 1.95 Å arising from the interaction between the Li—O atom of Li₂CO₃ and Co—O of Co₃O₄ catalyst (Figure 4h). It can be further corroborated by the charge density shift from the positive Li atom to the more electronegative O atom of Co₃O₄. Moreover, due to the observed distortion of the absorbed Li₂CO₃ structure on the composite catalyst, its

detachment from the catalyst surface during charging becomes easier, enabling the reversibility of the catalyst surface for further cycles (Figure 4i). The subsequent reaction mechanism studies reveal the discharge reaction to proceed through the formation of *LiCO₂ (Equation (1a,b)). Subsequently, another Li and CO₂ molecule combines with the intermediate product, Li₂C₂O₄, followed by subsequent disproportionation to form the discharge product *Li₂CO₃ and *CO (Equation (1c,d)). The adsorbed intermediate *CO subsequently disproportionates to form amorphous carbon and CO₂ (Figure 4j, Figure S19, Supporting Information, Equation (1e)).



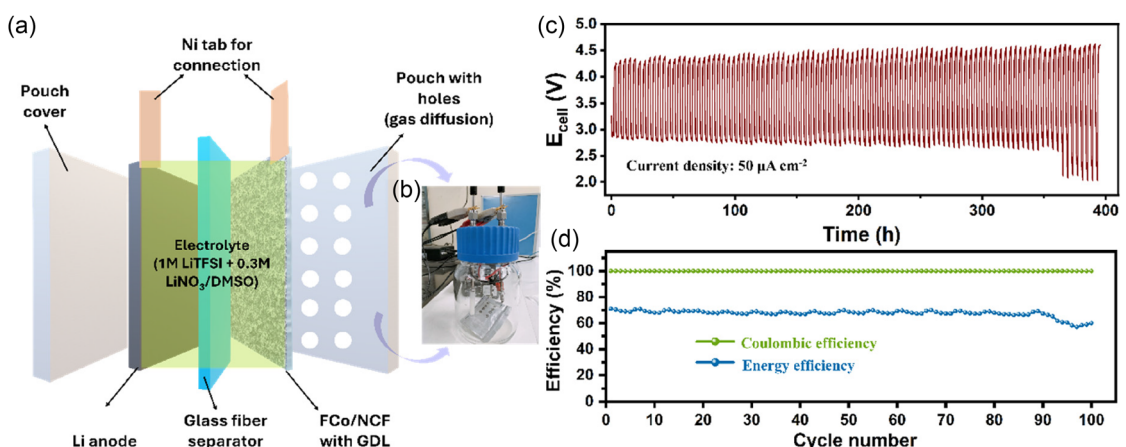


Figure 5. a) Schematic and b) setup of the pouch-cell Li-CO₂Mars battery. c) E versus t ; d) efficiency versus cycle number of the FCo/NCF-based Li-CO₂Mars battery.



Thus, the synergistic combination of the composite Fe₃O₄/Co₃O₄ along with the integration into the composite NCF leads to i) enhanced catalytic activity for CO₂RR and CO₂ER, ii) improved electronic conductivity of the nanofiber electrode enhancing the electron transfer, iii) higher CO₂ adsorption ability, and iv) improved stabilization of the discharge product Li₂CO₃ which significantly enhanced the electrochemical performance of the Li-CO₂Mars battery.

2.4. Demonstration of a Pouch Cell Li-CO₂Mars Battery

Although coin cell studies demonstrated improved electrochemical performance of the Li-CO₂Mars battery using the freestanding nanofiber electrodes, bringing the battery into real-life applications requires the scaling up of the system from the coin cell to the pouch cell scale. In this direction, we used a $3 \times 3 \text{ cm}^2$ electrospun FCo/NCF freestanding cathode and assembled it into a pouch cell, investigating the scalability of the designed catalyst-based Li-CO₂Mars battery (Figure 5a,b). The fabricated pouch cell was operated in a similar Martian gas composition at the current density of $50 \mu\text{A cm}^{-2}$ (0.45 mA calculated based on the area of the electrode) for a limited capacity of 0.1 mAh cm^{-2} . The designed cell could operate continuously for about 400 h and had a high cycling life of 100 cycles. Moreover, with the discharge voltage being greater than 2.5 V, it can be ascertained that even after scaling the system to the pouch cell level, the intrinsic catalytic activity of the freestanding catalyst-based electrodes for the CO₂RR and CO₂ER was maintained (Figure 5c).

Further, considering the practical applications, the gravimetric energy density of the developed pouch cell is significantly important. Considering the total mass of the assembled pouch Li-CO₂Mars battery and the limited discharge/charge specific capacity of 0.1 mAh cm^{-2} , a significantly high gravimetric energy density of 724.1 Wh kg^{-1} is obtained, substantially exceeding that of the conventional Li-ion batteries^[46] (Table S2). A high energy

efficiency of 71% was observed in the first cycle with the limited capacity, which, although decreased slightly with the number of cycles, still had an average of 68.3% efficiency even after 368 h of operation life, demonstrating the efficient operability of the Li-CO₂Mars batteries using the synthesized freestanding FCo/NCF catalyst (Figure 5d). The developed catalyst, along with the scaled-up prototype pouch cell Li-CO₂Mars battery, provides a cost-effective, high-energy density and an environment-friendly pathway toward the utilization of the system for large-scale applications both on Earth and Mars.

3. Conclusions

In summary, we developed a unique composite catalyst of MOF-derived Fe₃O₄/Co₃O₄ composite nanoparticles embedded into the electrospun N-doped carbon nanofibers as a freestanding catalytic electrode for the Li-CO₂Mars battery. The synergistic combination of the nanoparticles and the nanofiber network provided the advantages of i) uniform distribution of the catalyst nanoparticles without any agglomeration, ensuring a large number of catalytically active sites along with enhanced catalytic activity for CO₂RR and CO₂ER; ii) an electrically conductive network of the nanofibers, ensuring efficient electron transfer from the reaction sites to the external circuit and vice versa; iii) elimination of the usage of insulating binder, thus mitigating the side reactions between the binder and the reactive intermediates; and iv) the scalability for large-scale applications by directly integrating the catalyst into the electrodes. Because of these improvements, the FCo/NCF-based freestanding Li-CO₂Mars coin cells could efficiently operate for a cycling life of 120 cycles at the high current density of $50 \mu\text{A cm}^{-2}$ for the limited discharge/charge capacity of 0.1 mAh cm^{-2} having a nearly constant overpotential of 1.57 V even after 80 cycles and cycle life of 60 cycles, even after an increase of the limited discharge/charge capacity to 0.25 mAh cm^{-2} . In addition, a significantly high full discharge capacity of 6.8 mAh cm^{-2} and a Coulombic efficiency of 71.5% were delivered by the developed system. The ex situ physicochemical characterization techniques,

along with the *in situ* Raman spectroscopy and theoretical studies, confirmed the discharge/charge reactions. They involved the formation and breakdown of the amorphous carbon as per the reaction, $4\text{Li}^+ + 3\text{CO}_2 \leftrightarrow 2\text{Li}_2\text{CO}_3 + \text{C}$. Thereafter, the coin-cell-based system is scaled up to develop the first prototype Li-CO₂Mars pouch cell efficiently operating in the Martian gas atmosphere with an average energy efficiency of >68% and a significantly high energy density of 724.1 Wh kg⁻¹. The unique, scalable freestanding catalyst electrode provides a versatile approach and advances expertise toward the development of Li-CO₂Mars battery beyond the coin cells. This will enable its utilization as an energy storage system in a wide range of applications, ranging from integration with CO₂-producing sources on Earth to rover missions on Mars.

4. Experimental Section

Synthesis of ZIF-67 and Fe-ZIF-67

ZIF-67 particles were synthesized as per previous reports.^[47] Briefly, 4 mmol of Co(NO₃)₂·6H₂O (Sigma-Aldrich, 99.9% trace metals basis) and 12 mmol of 2-methylimidazole (MIM) (Sigma-Aldrich) were dissolved in 30 mL of methanol separately under continuous stirring for about 0.5 h. Subsequently, the two solutions were mixed and aged for 12 h at room temperature ($\approx 25^\circ\text{C}$) under stirring. The obtained ZIF-67 particles were centrifuged and washed with methanol several times to remove the unreacted reactants, followed by overnight vacuum drying at 60 °C to obtain the final particles.

The bimetallic Fe-ZIF-67 particles were synthesized through an ion-displacement reaction in ZIF-67. In brief, 0.25 g of the synthesized ZIF-67 and 0.15 g of K₃[Fe(CN)₆] (Sigma-Aldrich, 99%) were added into a solution of 125 mL of methanol and 25 mL of distilled water, respectively. The solutions were then mixed under vigorous stirring for 3 h, followed by centrifugal washing with methanol and subsequent drying under vacuum at 60 °C to obtain Fe-ZIF-67.

Synthesis of N-Doped Carbon Nanofibers

The polyacrylonitrile (PAN, M.W.: 150 000, Sigma-Aldrich) nanofibers were synthesized using the electrospinning technique. To synthesize NCF, 0.456 g of PAN was dissolved in 5 mL N,N-dimethyl formamide (DMF) (SRL Pvt. Ltd., 99.5%) under stirring to obtain a viscous solution (electrospinning solution). The solution is then loaded into a syringe, followed by electrospinning at a flow rate of 1 mL h⁻¹ at 15 kV voltage. The spinneret and the collector were kept at a distance of 15 cm, and the humidity in the electrospinning chamber was maintained in the range of 25–30%. The resulting PAN-nanofibers are collected on an aluminum substrate. The fibers are then heat treated in two stages in an air atmosphere, first at 150 °C for 2 h (heating rate: 2 °C min⁻¹), followed by the next stage at 280 °C for 2 h at the same heating rate. The heat-treated fibers are then pyrolyzed in an N₂ atmosphere at 900 °C for 1 h to obtain NCF.

Synthesis of Co₃O₄/NCF (Co/NCF)

The Co/NCF was synthesized similarly to NCF except with the addition of ZIF-67. 45.6 mg of the synthesized ZIF-67 was added to a solution of 0.456 g PAN in 5 mL DMF under stirring to obtain a viscous solution. The electrospinning procedure followed by heat treatment and pyrolysis, as in the case of NCF, was used to obtain the Co/NCF.

Synthesis of Fe₃O₄/Co₃O₄/NCF (FCo/NCF)

To obtain the FCo/NCF, 45.6 mg of the synthesized Fe-ZIF-67 and 0.456 g of PAN in 5 mL DMF were dissolved under stirring to obtain a viscous solution. The obtained solution was electrospun, heat treated, and pyrolyzed in conditions similar to the previous nanofibers to obtain the FCo/NCF.

Batteries Assembly and Electrochemical Measurements

The different carbon fiber mats were punched into 15 mm diameter circular discs (\approx average weight of 2.4 mg) and used as cathode along with carbon paper (thickness 0.4 mm, porosity 78%, density 0.44 g cm⁻³) as the gas diffusion layer. Li-metal foil (15 mm diameter, 0.38 mm thickness) (99%, Sigma-Aldrich) was used as the anode, 1 M LiTFSI + 0.3 M LiNO₃ in DMSO as the electrolyte, and a glass fiber membrane of thickness 675 µm (Whatman, GF/D; Global Life Sciences Solutions) as the separator. The Li-CO₂Mars battery was assembled in a glove box (H₂O: <0.1 ppm, O₂: <0.1 ppm) using a CR2032-type coin cell with holes on the cathode side to allow the entry of CO₂Mars gas. The assembled coin cell was then sealed in a glass bottle, which was purged by the Martian gas (Martian gas (CO₂Mars): 95% CO₂, 2.6% N₂, 1.9% Ar, 0.16% O₂, and 0.06% CO by volume, SVCGPL).

The pouch cell was assembled using a fiber mat (3 × 3 cm) with a thickness similar to that used in the coin cell, along with Ni foam of the same dimensions as the gas diffusion layer. A Li metal (2 × 2 cm) with a thickness of 1.5 mm as the anode with Ni-tabs for external connections and the same electrolyte-soaked glass fiber paper as the separator. The assembly was sealed in a laminated aluminum pouch with six holes on the cathode side to ensure the diffusion of the CO₂Mars gas into the battery. The potentiostat (Biologic BCS-805) was used to examine the electrochemical performances of the CR2032 coin cells at various experimental conditions. EIS analysis was performed in the frequency range of 10 kHz to 100 mHz. Pouch cells were investigated using the NanoCycler (Make: NANOBASE) under different experimental conditions. The applied areal current and discharge/charge capacity in this work are calculated based on the area of the electrode. The *in situ* Raman measurements were carried out in the ECC-Opto-Gas cell (Make: EL-Cell GmbH) with the freestanding electrode and Li metal as the anode. The assembled cell was connected to the NanoCycler for electrochemical operation, and the corresponding Raman spectra were obtained using the Raman microscope, as described in the materials characterization section.

Acknowledgements

CSS acknowledges the financial support from the Department of Science and Technology, Government of India, and SERB through the DST Swarnajayanti Fellowship, 2020 (Project No. DST/SJF/ETA-02/2019-20). The authors acknowledge the National Supercomputing Mission (NSM) for providing computing resources of “PARAM SEVA” at IIT, Hyderabad, which is implemented by C-DAC and supported by the Ministry of Electronics and Information Technology (MeitY) and Department of Science and Technology (DST), Government of India.

Conflict of Interest

The authors declare no conflict of interest.

Author Contributions

Ankit Kumar Chourasia: conceptualization (lead); data curation (equal); formal analysis (equal); investigation (equal); methodology (lead); validation (equal); visualization (equal); writing—original draft (equal). **Keerti M. Naik:** data curation (equal); investigation (equal); validation (equal); visualization (equal); writing—original draft (equal). **Chandra S. Sharma:** funding acquisition (lead); project administration (lead); supervision (lead); writing—review and editing (supporting).

Data Availability Statement

The data that support the findings of this study are available from the corresponding author upon reasonable request.

Keywords: core-shell • freestanding electrodes • Li-CO₂Mars batteries • metal–organic frameworks • pouch cells

- [1] A. Sarkar, V. R. Dharmaraj, C.-H. Yi, K. Iputera, S.-Y. Huang, R.-J. Chung, S.-F. Hu, R.-S. Liu, *Chem. Rev.* **2023**, *123*, 9497.
- [2] J. Li, L. Wang, Y. Zhao, S. Li, X. Fu, B. Wang, H. Peng, *Adv. Funct. Mater.* **2020**, *30*, 2001619.
- [3] K. M. Naik, A. Kumar Chourasia, C. S. Sharma, *Chem. Eng. J.* **2024**, *490*, 151729.
- [4] Y. Jin, Y. Liu, L. Song, J. Yu, K. Li, M. Zhang, J. Wang, *Chem. Eng. J.* **2022**, *430*, 133029.
- [5] Z. Cheng, Z. Wu, J. Chen, Y. Fang, S. Lin, J. Zhang, S. Xiang, Y. Zhou, Z. Zhang, *Small* **2023**, *19*, 2301685.
- [6] H. Wang, K. Xie, Y. You, Q. Hou, K. Zhang, N. Li, W. Yu, K. P. Loh, C. Shen, B. Wei, *Adv. Energy Mater.* **2019**, *9*, 1901806.
- [7] A. K. Chourasia, K. M. Naik, C. S. Sharma, *Carbon N. Y.* **2024**, *218*, 118754.
- [8] P.-F. Zhang, Y.-Q. Lu, Y.-J. Wu, Z.-W. Yin, J.-T. Li, Y. Zhou, Y.-H. Hong, Y.-Y. Li, L. Huang, S.-G. Sun, *Chem. Eng. J.* **2019**, *363*, 224.
- [9] X. Li, J. Zhang, G. Qi, J. Cheng, B. Wang, *Energy Storage Mater.* **2021**, *35*, 148.
- [10] W. Yu, L. Liu, Y. Yang, N. Li, Y. Chen, X. Yin, J. Niu, J. Wang, S. Ding, *Chem. Eng. J.* **2023**, *465*, 142787.
- [11] X. Li, J. Zhou, J. Zhang, M. Li, X. Bi, T. Liu, T. He, J. Cheng, F. Zhang, Y. Li, X. Mu, J. Lu, B. Wang, *Adv. Mater.* **2019**, *31*, 1903852.
- [12] T. Hu, W. Lian, K. Hu, Q. Li, X. Cui, T. Yao, L. Shen, *Nano-Micro Lett.* **2024**, *17*, 5.
- [13] K. Hu, T. Hu, T. Yao, X. Cui, Q. Li, L. Shen, *ACS Nano* **2025**, *19*, 7707.
- [14] Z. Wang, B. Liu, X. Yang, C. Zhao, P. Dong, X. Li, Y. Zhang, K. Doyle-Davis, X. Zeng, Y. Zhang, X. Sun, *Adv. Funct. Mater.* **2023**, *33*, 2213931.
- [15] T. Jian, W. Ma, J. Hou, J. Ma, X. Li, H. Gao, C. Xu, H. Liu, *Nano Res.* **2024**, *17*, 5206.
- [16] J. Wang, N. Feng, S. Zhang, Y. Lin, Y. Zhang, J. Du, S. Tian, Q. Zhao, G. Yang, *Adv. Sci.* **2024**, *11*, 2402892.
- [17] Y. Liu, P. Shu, M. Zhang, B. Chen, Y. Song, B. Lu, R. Mao, Q. Peng, G. Zhou, H.-M. Cheng, *ACS Energy Lett.* **2024**, *9*, 2173.
- [18] X.-Y. Kong, X.-H. Liang, X.-B. Yang, W.-Z. Sun, Q.-C. Zhu, *Electrochim. Acta* **2024**, *488*, 144236.
- [19] H. Wang, R. Zheng, C. Shu, J. Long, *ChemElectroChem* **2020**, *7*, 4922.
- [20] C.-J. Chen, C.-S. Huang, Y.-C. Huang, F.-M. Wang, X.-C. Wang, C.-C. Wu, W.-S. Chang, C.-L. Dong, L.-C. Yin, R.-S. Liu, *ACS Appl. Mater. Interfaces* **2021**, *13*, 6156.
- [21] Z. Hu, Y. Xie, D. Yu, Q. Liu, L. Zhou, K. Zhang, P. Li, F. Hu, L. Li, S. Chou, S. Peng, *ACS Nano* **2021**, *15*, 8407.
- [22] Z. Lian, Y. Lu, C. Wang, X. Zhu, S. Ma, Z. Li, Q. Liu, S. Zang, *Adv. Sci.* **2021**, *8*, 2102550.
- [23] K. Shang, W. Li, Y. Liu, W. Zhang, H. Yang, J. Xie, Z. Liu, S.-L. Chou, L. Zhao, R. Zeng, *RSC Adv.* **2015**, *5*, 70527.
- [24] P. Wang, C. Jin, X. Pang, W. Zheng, G. Gao, D. Wang, D. Zheng, H. Dai, H. Bai, *Appl. Surf. Sci.* **2019**, *493*, 1236.
- [25] Y. Li, Y. Xu, W. Yang, W. Shen, H. Xue, H. Pang, *Small* **2018**, *14*, 1704435.
- [26] N. Cheng, L. Ren, X. Xu, Y. Du, S. X. Dou, *Adv. Energy Mater.* **2018**, *8*, 1801257.
- [27] K. M. Naik, A. K. Chourasia, C. S. Sharma, *J. Power Sources* **2024**, *608*, 234623.
- [28] A. K. Chourasia, M. Shavez, K. M. Naik, C. Bongu, C. S. Sharma, *ACS Appl. Energy Mater.* **2023**, *6*, 378.
- [29] T. Hu, Y. Hu, T. Yao, K. Hu, X. Cui, Q. Li, L. Shen, *Energy Storage Mater.* **2024**, *72*, 103740.
- [30] E. Nasibulin, W. Xu, M. H. Engelhard, Z. Nie, X. S. Li, J.-G. Zhang, *J. Power Sources* **2013**, *243*, 899.
- [31] J. K. Papp, J. D. Forster, C. M. Burke, H. W. Kim, A. C. Luntz, R. M. Shelby, J. J. Urban, B. D. McCloskey, *J. Phys. Chem. Lett.* **2017**, *8*, 1169.
- [32] Q. Chen, X. Zhang, S. Li, J. Tan, C. Xu, Y. Huang, *Chem. Eng. J.* **2020**, *395*, 125130.
- [33] J. Zhang, J. Qian, J. Ran, P. Xi, L. Yang, D. Gao, *ACS Catal.* **2020**, *10*, 12376.
- [34] J. Wu, X. Sun, H. Chen, S. Guo, D. Hou, D. Wang, H. Wang, *Energy Fuels* **2024**, *38*, 7218.
- [35] F. E. Che Othman, N. Yusof, H. Hasbullah, J. Jaafar, A. F. Ismail, N. Abdullah, N. A. H. Md Nordin, F. Aziz, W. N. Wan Salleh, *J. Ind. Eng. Chem.* **2017**, *51*, 281.
- [36] J. Li, Y. Liang, B. Dou, C. Ma, R. Lu, Z. Hao, Q. Xie, Z. Luan, K. Li, *Mater. Chem. Phys.* **2013**, *138*, 484.
- [37] A. E. Danks, M. J. Hollamby, B. Hammouda, D. C. Fletcher, F. Johnston-Banks, S. E. Rogers, Z. Schnepf, *J. Mater. Chem. A* **2017**, *5*, 11644.
- [38] R. D. Hunter, J. Ramírez-Rico, Z. Schnepf, *J. Mater. Chem. A* **2022**, *10*, 4489.
- [39] C. Thambiliyagodage, S. Nakandala, B. Siriwardana, B. Lansakara, *Carbon Trends* **2021**, *5*, 100130.
- [40] S. R. Dhakate, A. Gupta, A. Chaudhari, J. Tawale, R. B. Mathur, *Synth. Met.* **2011**, *161*, 411.
- [41] T. Wang, Z. Chen, W. Gong, F. Xu, X. Song, X. He, M. Fan, *ACS Omega* **2023**, *8*, 22316.
- [42] M. Thommes, K. Kaneko, A. V. Neimark, J. P. Olivier, F. Rodriguez-Reinoso, J. Rouquerol, K. S. W. Sing, *Pure Appl. Chem.* **2015**, *87*, 1051.
- [43] B. J. Tan, K. J. Klabunde, P. M. A. Sherwood, *Chem. Mater.* **1990**, *2*, 186.
- [44] N. Jiang, J. Song, M. Yan, Y. Hu, M. Wang, Y. Liu, M. Huang, *Bioresour. Technol.* **2023**, *367*, 128230.
- [45] S. Yang, P. He, H. Zhou, *Energy Environ. Sci.* **2016**, *9*, 1650.
- [46] C. Wang, C. Yang, Z. Zheng, *Adv. Sci.* **2022**, *9*, 2105213.
- [47] X. Gong, T. Yang, Y. Song, X. Tian, Z. Ma, Z. Liu, *Compos. Sci. Technol.* **2024**, *247*, 110403.

Manuscript received: March 26, 2025

Revised manuscript received: May 14, 2025

Version of record online: